

1 **Tropopause Evolution in a Rapidly Intensifying Tropical Cyclone: A Static**  
2 **Stability Budget Analysis**

3 Patrick Duran\* and John Molinari

4 *University at Albany, State University of New York, Albany, NY*

5 \**Corresponding author address:* Department of Atmospheric and Environmental Sciences, Univer-  
6 sity at Albany, State University of New York, 1400 Washington Avenue, Albany, NY.

7 E-mail: pduran2008@gmail.com

## ABSTRACT

<sup>8</sup> We have some cool results!

## 9 **1. Introduction**

10 After undergoing a remarkably rapid intensification (RI), Hurricane Patricia (2015) set a new  
11 record as the strongest tropical cyclone (TC) ever observed in the Western Hemisphere (Kim-  
12 berlain et al. 2016; Rogers et al. 2017). High-altitude dropsonde observations taken during  
13 the Tropical Cyclone Intensity (TCI) experiment captured this RI in unprecedented detail (Doyle  
14 et al. 2017). These observations revealed remarkable changes in the structure of the cold-point  
15 tropopause and upper-level static stability as the storm intensified (Duran and Molinari 2018).

16 At tropical storm intensity, shortly before RI commenced, a strong inversion layer existed just  
17 above Patricia’s cold-point tropopause, which was located near 17.2 km. During the first half of  
18 the RI period, this inversion layer weakened throughout Patricia’s inner core, with the weakening  
19 most pronounced over the developing eye. By the time the storm reached its maximum intensity,  
20 the inversion layer over the eye had disappeared almost completely, which was accompanied by an  
21 increase in the tropopause height to a level at or above the highest-available dropsonde data point  
22 (18.3 km) at two locations. Meanwhile over the eyewall region, the static stability re-strengthened  
23 and the tropopause was limited to a level at or below 17.5 km. The mechanisms that led to these  
24 changes in upper-level static stability and tropopause height are the subject of the current paper.

25 Despite the importance of tropopause-layer thermodynamics in theoretical models of hurricanes  
26 (Emanuel and Rotunno 2011; Emanuel 2012), few papers have examined the upper-tropospheric  
27 evolution of TCs. Komaromi and Doyle (2017) found that stronger TCs tended to have a higher  
28 and warmer tropopause over their inner core than weaker TCs. Their results are consistent with  
29 the evolution observed over the inner core of Hurricane Patricia, in which the tropopause height  
30 increased and the tropopause temperature warmed throughout RI (Duran and Molinari 2018). The  
31 simulations of Ohno and Satoh (2015) suggested that the development of an upper-level warm core

32 within the eye acted to decrease the static stability near the tropopause. Although the mechanisms  
33 that drive this static stability evolution have not been examined explicitly, the potential temperature  
34 ( $\theta$ ) budget analysis of Stern and Zhang (2013) examined the development of the TC warm core.  
35 They found that radial and vertical advection both play important roles in warm core development  
36 throughout RI, with subgrid-scale diffusion becoming particularly important during the later stage  
37 of RI.

38 The analysis herein is based upon that of Stern and Zhang (2013), except using a static stability  
39 budget similar to that of Kepert et al. (2016) rather than a  $\theta$  budget.

## 40 **2. Model Setup**

41 The numerical simulations were performed using version 19.4 of Cloud Model 1 (CM1) de-  
42 scribed in Bryan and Rotunno (2009). The equations of motion were integrated on a 3000-km-  
43 wide, 30-km-deep axisymmetric grid with 1-km horizontal and 250-m vertical grid spacing. The  
44 computations were performed on an  $f$ -plane at 15°N latitude, over a sea surface with constant  
45 temperature of 30.5°C, which matches that observed near Hurricane Patricia (2015; Kimberlain  
46 et al. 2016). Horizontal turbulence was parameterized using the Smagorinsky scheme described in  
47 Bryan and Rotunno (2009, pg. 1773), with a prescribed mixing length that varied linearly from 100  
48 m at a surface pressure of 1015 hPa to 1000 m at a surface pressure of 900 hPa. This formulation  
49 allows for realistically-large horizontal mixing lengths near the hurricane’s inner core, consistent  
50 with the results of Bryan (2012), while not over-representing horizontal turbulence in convection  
51 at outer radii. Vertical turbulence was parameterized using the formulation of Markowski and  
52 Bryan (2016, their Eq. 6), using an asymptotic vertical mixing length of 100 m. A Rayleigh  
53 damping layer was applied outside of the 2900-km radius and above the 25-km level to prevent  
54 spurious gravity wave reflection at the model boundaries. Microphysical processes were param-

eterized using the Thompson et al. (2004) microphysics scheme and radiative heating tendencies were computed every two minutes using the Rapid Radiative Transfer Model for GCMs (RRTMG) longwave and shortwave schemes (Iacono et al. 2008). The initial temperature and humidity field was horizontally homogeneous and determined by averaging all Climate Forecast System Reanalysis (CFSR) grid points within 100 km of Patricia’s center of circulation at 18 UTC 21 October 2015. The vortex described in Rotunno and Emanuel (1987, their Eq. 37) was used to initialize the wind field, setting all parameters equal to the values used therein.

Although hurricanes simulated in an axisymmetric framework tend to be more intense than those observed in nature, the intensity evolution of this simulation matches reasonably well with that observed in Hurricane Patricia. After an initial spin-up period of about 20 hours, the modeled storm (Fig.1, blue lines) began an RI period that lasted approximately 30 hours. After this RI, the storm continued to intensify more slowly until the maximum 10-m wind speed reached  $89 \text{ m s}^{-1}$  and the minimum sea-level pressure reached its minimum of 846 mb, 81 hours into the simulation. Hurricane Patricia (red stars) exhibited a similar intensity evolution, with an RI period leading to a maximum 10-m wind speed of  $95 \text{ m s}^{-1}$  and a minimum sea-level pressure of 872 hPa. Despite the limitations of the axisymmetric framework, the extraordinary intensity of Hurricane Patricia and the rapidity of its intensification makes Patricia a particularly good candidate for axisymmetric analysis.

### 3. Budget Computation

The static stability can be expressed as the squared Brunt Väisälä frequency:

$$N_m^2 = \frac{g}{T} \left( \frac{\partial T}{\partial z} + \Gamma_m \right) \left( 1 + \frac{T}{R_d/R_v + q_s} \frac{\partial q_s}{\partial T} \right) - \frac{g}{1 + q_t} \frac{\partial q_t}{\partial z}, \quad (1)$$

75 where  $g$  is gravitational acceleration,  $T$  is temperature,  $R_d$  and  $R_v$  are the gas constants of dry air  
 76 and water vapor, respectively,  $q_s$  is the saturation mixing ratio,  $q_t$  is the total condensate mixing  
 77 ratio, and  $\Gamma_m$  is the moist-adiabatic lapse rate:

$$\Gamma_m = g(1 + q_t) \left( \frac{1 + L_v q_s / R_d T}{c_{pm} + L_v \partial q_s / \partial T} \right), \quad (2)$$

78 where  $L_v$  is the latent heat of vaporization and  $c_{pm}$  is the specific heat of moist air at constant  
 79 pressure. In the tropopause layer,  $q_s$ ,  $\partial q_s / \partial T$ , and  $\partial q_t / \partial z$  approach zero. In this limiting case,  
 80 Eq. 1 reduces to:

$$N^2 = \frac{g}{\theta} \frac{\partial \theta}{\partial z}, \quad (3)$$

81 where  $\theta$  is the potential temperature.

82 To compute  $N^2$ , CM1 uses Eq.1 in saturated environments and Eq. 3 in sub-saturated environ-  
 83 ments. For simplicity, however, only Eq. 3 will be employed for the budget computations herein<sup>1</sup>.

84 Taking the time derivative of Eq. 3 yields the static stability tendency:

$$\frac{\partial N^2}{\partial t} = \frac{g}{\theta} \frac{\partial}{\partial z} \frac{\partial \theta}{\partial t} - \frac{g}{\theta^2} \frac{\partial \theta}{\partial z} \frac{\partial \theta}{\partial t}, \quad (4)$$

85 where the potential temperature tendency,  $\partial \theta / \partial t$ , can be written:

$$\frac{\partial \theta}{\partial t} = HADV + VADV + HTURB + VTURB + MP + RAD + DISS \quad (5)$$

86 Each term on the right-hand side of Eq. 5 represents a  $\theta$  budget variable, each of which is out-  
 87 put directly by the model every minute. HADV and VADV are the radial and vertical advective  
 88 tendencies, HTURB and VTURB are the radial and vertical tendencies from the turbulence pa-  
 89 rameterization, MP is the tendency from the microphysics scheme, RAD is the tendency from the  
 90 radiation scheme, and DISS is the tendency due to turbulent dissipation. This equation neglects  
 91 Rayleigh damping, since this term is zero everywhere below 25 km, and the analysis domain does

---

<sup>1</sup>The validity of this approximation will be substantiated later in this section.

not extend to that level. Each term in Eq. 5 is substituted for  $\partial\theta/\partial t$  in Eq. 4, yielding the contribution of each budget term to the static stability tendency. These terms are summed, yielding an instantaneous "budget change" in  $N^2$  every minute. The budget changes are then averaged over 24-hour periods and compared to the total model change in  $N^2$  over that same time period, i.e.:

$$\Delta N_{budget}^2 = \frac{1}{\delta t} \sum_{t=t_0}^{t_0+\delta t} \frac{\partial N^2}{\partial t} \bigg|_t \quad (6)$$

$$\Delta N_{model}^2 = N_{t_0+\delta t}^2 - N_{t_0}^2 \quad (7)$$

$$Residual = \Delta N_{model}^2 - \Delta N_{budget}^2 \quad (8)$$

where  $t_0$  is an initial time and  $\delta t$  is 24 hours.

Eqs. 6-8 are plotted for four consecutive 24-hour periods in Fig. 2. For this and all subsequent radial-vertical cross sections, a 1-2-1 smoother is applied once in the radial direction to eliminate  $2\Delta r$  noise that appears in some of the raw model output and calculated fields. The left column of Fig. 2 depicts the model changes (Eq. 7), the center column depicts the budget changes (Eq. 6), and the right column depicts the residuals (Eq. 8). In every 24-hour period, the budget changes are nearly identical to the model changes, which is reflected in the near-zero residuals in the right column. This indicates that the budget accurately represents the model variability, which implies that the neglect of moisture in the budget computation introduces negligible error within the analysis domain<sup>2</sup>.

In the tropopause layer, some of the budget terms are small enough to be ignored. To determine which of the budget terms are most important, a time series of the contribution of each of the budget terms in Eq. 5 to the tropopause-layer static stability tendency is plotted in Fig. 4. For this figure, each of the budget terms is computed using the method described in Section 3, except with

---

<sup>2</sup>This is not the case in the lower- and mid-troposphere, where the residual actually exceeds the budget variability in many places, likely due to the neglect of moisture; thus we limit this analysis to the upper troposphere and lower stratosphere.

112 1-hour averaging intervals instead of 24-hour intervals. The absolute values of these tendencies  
113 are then averaged over a radius-height domain surrounding the tropopause and plotted as a time  
114 series<sup>3</sup>. Advection (Fig. 4, red line) plays an important role in the mean tropopause-layer static  
115 stability tendency at all times, and vertical turbulence (Fig. 4, blue line) and radiation (Fig. 4, dark  
116 green line) also contribute significantly. Although the contribution from horizontal turbulence  
117 (Fig. 4, purple line) becomes more important after 48 hours, it is confined to a very small region  
118 immediately surrounding the eyewall tangential velocity maximum (not shown), and is negligible  
119 throughout the rest of the tropopause layer. The remaining two processes - microphysics and  
120 dissipative heating (Fig. 4, orange and light green lines, respectively) - lie atop one another near  
121 zero. These time series indicate that, at all times, three budget terms dominate the tropopause-layer  
122 static stability tendency: advection, vertical turbulence, and radiation. Variations in the magnitude  
123 and spatial structure of these terms drive the static stability changes depicted in Fig. 2; subsequent  
124 sections will focus on these variations and what causes them.

## 125 4. Results

### 126 a. Static stability evolution

127 The average  $N^2$  over the first day of the simulation (Fig. 3a) indicates the presence of a weak  
128 static stability maximum just above the cold-point tropopause. Over the subsequent 24 hours,  
129 during the RI period, the static stability within and above this layer decreased near the storm  
130 center (Fig. 3b). This decreasing  $N^2$  corresponded to an increase in the tropopause height within  
131 the developing eye, maximized at the storm center. Outside of the eye, meanwhile, the tropopause

---

<sup>3</sup>It will be seen in subsequent figures that each of the terms contributes both positively and negatively to the  $N^2$  tendency within the analysis domain. Thus, taking an average over the domain tends to wash out the positive and negative contributions. To circumvent this problem, the absolute value of each of the terms is averaged.



height decreased over the eyewall region (25-60-km radius) and increased only slightly outside of the 60-km radius. In this outer region, the  $N^2$  maximum just above the tropopause strengthened during RI. These trends continued as the storm's intensity leveled off in the 48-72-hour period (Fig. 3c). The tropopause height increased to nearly 21 km at the storm center and sloped sharply downward to 16.3 km on the inner edge of the eyewall, near the 30 km radius. Static stability outside of the eye, meanwhile, continued to increase just above the cold-point tropopause. This  $N^2$  evolution closely follows that observed in Hurricane Patricia (2015; Duran and Molinari 2018). The mechanisms that led to these static stability changes will be investigated in the subsequent sections.

#### *b. Static stability budget analysis*

*(i) 0-24 hours* The weakening of the lower-stratospheric static stability maximum during the initial spin-up period is reflected in the total  $N^2$  budget change over this time (Fig. 5a). The 17-18-km layer was characterized by decreasing  $N^2$  (purple shading), maximizing at the storm center. The layer immediately below the tropopause, meanwhile, saw strengthening  $N^2$  during this time period. Although these tendencies extended out to the 200-km radius, they were particularly pronounced at innermost radii. A comparison of the contributions of advection (Fig. 5b), vertical turbulence (Fig. 5c), and radiation (Fig. 5d) reveals that advection is primarily responsible for the change in static stability during this period. Although vertical turbulence acts in opposition to advection (i.e. it acts to stabilize regions that advection acts to destabilize), the magnitude of the advective tendencies is larger, particularly at the innermost radii. The sum of advection and vertical turbulence (Fig. 5e) almost exactly replicates the static stability tendencies above 17 km. Radiative tendencies (Fig. 5d) act to destabilize the layer below about 16 km and stabilize the

154 layer between 16 and 17 km. The sum of advection, vertical turbulence, and radiation (Fig. 5f)  
155 reproduces the total change in  $N^2$  almost exactly.

156 ...Explain this in the context of radial and vertical velocities... ...See Stern and Zhang, Page 84,  
157 Section 3d... ...Add mention of total condensate and radiative heating tendencies as it relates to  
158 stability tendency due to rad...

159 (ii) *24-48 hours* During the RI period within the eye,  $N^2$  generally decreased above 16 km and  
160 increased below (Fig. 6a). These tendencies at the innermost radii were driven almost entirely  
161 by advection (Fig. 6b); vertical turbulence (Fig. 6c) and radiation (Fig. 6d) contributed negligibly  
162 to the static stability tendencies in this region. Outside of the eye, meanwhile, the  $N^2$  evolution  
163 exhibited alternating layers of positive and negative tendencies. Near and above 18 km existed an  
164 upward-sloping region of decreasing  $N^2$  that extended out to the 180-km radius. In this region,  
165 neither vertical turbulence nor radiation exhibited negative  $N^2$  tendencies; advection was the only  
166 forcing for destabilization. Immediately below this layer was a region of increasing  $N^2$ , which  
167 sloped upward from 17 km near the 30-km radius to just below 18 km outside of the 100 km radius.  
168 Advection and vertical turbulence both contributed to this positive  $N^2$  tendency, with advection  
169 playing an important role below about 17.5 km and and turbulence playing an important role above.  
170 The sum of advection and turbulence (Fig. 6e) reveals two discontinuous regions of increasing  
171  $N^2$  rather than one contiguous region. The addition of radiation to these two terms, however,  
172 (Fig. 6f) provides the link between these two regions, indicating that radiation also plays a role in  
173 strengthening the stable layer just above the tropopause. Below 17 km, a horizontally-extensive  
174 layer of decreasing  $N^2$  also was forced by a combination of advection, vertical turbulence, and  
175 radiation. The sum of advection and vertical turbulence accounts only for two isolated regions of  
176 decreasing  $N^2$  in this layer, and actually forces stabilization in part of the region. For example, just

177 above 16 km in the 150-200-km radial band, the sum of advection and vertical turbulence forces  
178 an increase in  $N^2$ . Likewise, throughout most of the 30-60-km radial band in this layer, advection  
179 and vertical turbulence combine to force near-zero or positive  $N^2$  tendencies. Radiative tendencies  
180 overcome this forcing for stabilization in both of these regions to produce the radially-extensive  
181 region of destabilization just below the tropopause.

182 TWO REGIONS WHERE Panel (f) differs from panel (a): 30-60 km radial band below 16 km,  
183 which is actually canceled out by a vertical gradient of latent heating, and the thin region of strong  
184 stabilization between 15-17.5 km near  $r=30$  km, which is canceled out by horizontal turbulence.

185 (iii) 48-72 hours The third day of the simulation marked a dramatic change in the structure of the  
186 tropopause-layer static stability tendencies. During this time, static stability increased markedly  
187 in an upward-sloping region within the 30-60-km radial band (Fig. 7a), and also increased within  
188 the 16.75-17.5-km layer out to at least the 200-km radius. As this layer stabilized, the layer  
189 immediately below it destabilized in a broad region extending from 60-200 km. Examination  
190 of the contribution from total advection (Fig. 7b) reveals that advection no longer dominates the  
191 static stability tendencies. Instead, a combination of vertical turbulence (Fig. 7c) and radiation  
192 (Fig. 7d) overcomes the destabilizing influence of advection to create the layer of increasing static  
193 stability. Meanwhile, the destabilizing influence of vertical turbulence in a broad region below  
194 17 km combines with a small region of destabilization due to radiation in the 50-120-km radial  
195 band combine to destabilize the layer below 16.5 km in the 50-200-km radial band. Comparing  
196 the sum of advection and vertical turbulence (Fig. 7e) to the sum of advection, vertical turbulence,  
197 and radiation (Fig. 7f) reveals that radiation plays a fundamental role in the re-strengthening of the  
198 lower-stratospheric stable layer during this time.

199 (iv) 72-96 hours

## 5. Discussion

Radiative heating and turbulence viscosity figures?

Discuss how turbulence increases the static stability in some regions – vertical gradients of turbulence intensity.

Dunion et al. speculate that the diurnal pulse only occurs in mature storms. Maybe the development of the near-tropopause stable layer could partially explain the reason for this.

*Acknowledgments.* We are indebted to George Bryan for his continued development and support of Cloud Model 1. We also thank Jeffrey Kepert, Robert Fovell, and Erika Navarro for helpful conversations related to this work. ADD GRANT NUMBER

## References

Bryan, G. H., 2012: Effects of surface exchange coefficients and turbulence length scales on the intensity and structure of numerically simulated hurricanes. *Mon. Wea. Rev.*, **140**, 1125–1143.

Bryan, G. H., and R. Rotunno, 2009: The maximum intensity of tropical cyclones in axisymmetric numerical model simulations. *Mon. Wea. Rev.*, **137**, 1770–1789.

Doyle, J. D., and Coauthors, 2017: A view of tropical cyclones from above: The Tropical Cyclone Intensity (TCI) Experiment. *Bull. Amer. Meteor. Soc.*, **98**, 2113–2134.

Duran, P., and J. Molinari, 2018: Dramatic inner-core tropopause variability during the rapid intensification of Hurricane Patricia (2015). *Mon. Wea. Rev.*, **XXX**, XXX–XXX.

Emanuel, K., 2012: Self-stratification of tropical cyclone outflow. part ii: Implications for storm intensification. *J. Atmos. Sci.*, **69**, 988–996.

220 Emanuel, K., and R. Rotunno, 2011: Self-stratification of tropical cyclone outflow. part i: Impli-  
 221 cations for storm structure. *J. Atmos. Sci.*, **68**, 2236–2249.

222 Iacono, M. J., J. S. Delamere, E. J. Mlawer, M. W. Shephard, S. A. Clough, and W. D. Collins,  
 223 2008: Radiative forcing by long-lived greenhouse gases: Calculations with the AER radiative  
 224 transfer models. *J. Geophys. Res.*, **113** (D13103).

225 Kepert, J. D., J. Schwendike, and H. Ramsay, 2016: Why is the tropical cyclone boundary layer  
 226 not "well mixed"? *J. Atmos. Sci.*, **73**, 957–973.

227 Kimberlain, T. B., E. S. Blake, and J. P. Cangialosi, 2016: Tropical cyclone report: Hurricane  
 228 Patricia. National Hurricane Center. [Available online at [www.nhc.noaa.gov](http://www.nhc.noaa.gov)].

229 Komaromi, W. A., and J. D. Doyle, 2017: Tropical cyclone outflow and warm core structure as  
 230 revealed by HS3 dropsonde data. *Mon. Wea. Rev.*, **145**, 1339–1359.

231 Markowski, P. M., and G. H. Bryan, 2016: LES of laminar flow in the PBL: A potential problem  
 232 for convective storm simulations. *Mon. Wea. Rev.*, **144**, 1841–1850.

233 Ohno, T., and M. Satoh, 2015: On the warm core of a tropical cyclone formed near the tropopause.  
 234 *J. Atmos. Sci.*, **72**, 551–571.

235 Rogers, R. F., S. Aberson, M. M. Bell, D. J. Cecil, J. D. Doyle, J. Morgerman, L. K. Shay, and  
 236 C. Velden, 2017: Re-writing the tropical record books: The extraordinary intensification of  
 237 Hurricane Patricia (2015). *Bull. Amer. Meteor. Soc.*, **98**, 2091–2112.

238 Rotunno, R., and K. A. Emanuel, 1987: An air-sea interaction theory for tropical cyclones. Part II:  
 239 Evolutionary study using a nonhydrostatic axisymmetric numerical model. *J. Atmos. Sci.*, **44**,  
 240 542–561.

241 Stern, D. P., and F. Zhang, 2013: How does the eye warm? part i: A potential temperature budget  
242 analysis of an idealized tropical cyclone. *J. Atmos. Sci.*, **70**, 73–89.

243 Thompson, G., R. M. Rasmussen, and K. Manning, 2004: Explicit forecasts of winter precipitation  
244 using an improved bulk microphysics scheme. Part I: Description and sensitivity analysis. *Mon.*  
245 *Wea. Rev.*, **132**, 519–542.

## LIST OF FIGURES

247	<b>Fig. 1.</b>	The maximum 10-m wind speed (top panel; $\text{m s}^{-1}$ ) and minimum sea-level pressure (bottom	
248		panel; hPa) in the simulated storm (blue lines) and from Hurricane Patricia's best track (red	
249		stars). . . . .	16
250	<b>Fig. 2.</b>	Left panels: Twenty-four-hour changes in squared Brunt-Väisälä frequency ( $N^2$ ; $10^{-4} \text{ s}^{-2}$ )	
251		over (a) 0-24 hours, (b) 24-48 hours, (c) 48-72 hours, (d) 72-96 hours. Middle Panels: The	
252		$N^2$ change over the same time periods computed using Eq. 6. Right Panels: The budget	
253		residual over the same time periods, computed by subtracting the budget change (middle	
254		column) from the model change (left column). . . . .	17
255	<b>Fig. 3.</b>	Twenty-four-hour averages of squared Brunt-Väisälä frequency ( $10^{-4} \text{ s}^{-2}$ ) over the first four	
256		days of the simulation. Orange lines represent the cold-point tropopause determined by the	
257		mean temperature field over the same time periods. . . . .	18
258	<b>Fig. 4.</b>	Time series of the contribution of each of the budget terms to the time tendency of the	
259		squared Brunt-Väisälä frequency ( $N^2$ ; $10^{-4} \text{ s}^{-2}$ ). For each budget term, the absolute value	
260		of the $N^2$ tendency is averaged temporally over 1-hour periods (using output every minute),	
261		and spatially in a region extending from 0 to 200 km radius and 14 to 21 km altitude. . . . .	19
262	<b>Fig. 5.</b>	(a) Total change in $N^2$ over the 0-24-hour period ( $10^{-4} \text{ s}^{-2} (24 \text{ hr})^{-1}$ ) and the contributions to	
263		that change from (b) the sum of horizontal and vertical advection, (c) vertical turbulence, (d)	
264		longwave and shortwave radiation, (e) the sum of horizontal advection, vertical advection,	
265		and vertical turbulence, and (f) the sum of horizontal advection, vertical advection, vertical	
266		turbulence, and longwave and shortwave radiation. . . . .	20

267	<b>Fig. 6.</b>	As in Fig. 5, but for the 24-48-hour period. . . . .	21
268	<b>Fig. 7.</b>	As in Fig. 5, but for the 48-72-hour period. . . . .	22
269	<b>Fig. 8.</b>	Radial velocity ( $\text{m s}^{-1}$ ; filled contours), potential temperature (K; thick black contours), and	
270		cold point tropopause height (orange lines) averaged over (a) 0-24 hours, (b) 24-48 hours,	
271		and (c) 48-72 hours. . . . .	23
272	<b>Fig. 9.</b>	Vertical velocity ( $\text{cm s}^{-1}$ ; filled contours), potential temperature (K; thick black contours),	
273		and cold point tropopause height (orange lines) averaged over (a) 0-24 hours, (b) 24-48	
274		hours, and (c) 48-72 hours. . . . .	24
275	<b>Fig. 10.</b>	Total condensate mixing ratio ( $\text{g kg}^{-1}$ ) and cold point tropopause height (orange lines) aver-	
276		aged over (a) 0-24 hours, (b) 24-48 hours, and (c) 48-72 hours. . . . .	25
277	<b>Fig. 11.</b>	Radiative heating rate ( $\text{K hr}^{-1}$ ) and cold point tropopause height (orange lines) averaged over	
278		(a) 0-24 hours, (b) 24-48 hours, and (c) 48-72 hours. . . . .	26
279	<b>Fig. 12.</b>	Vertical eddy diffusivity ( $\text{m}^2 \text{s}^{-2}$ ; filled contours), cold point tropopause height (cyan lines),	
280		and radial velocity ( $\text{m s}^{-1}$ ; thick black lines) averaged over (a) 0-24 hours, (b) 24-48 hours,	
281		and (c) 48-72 hours. . . . .	27



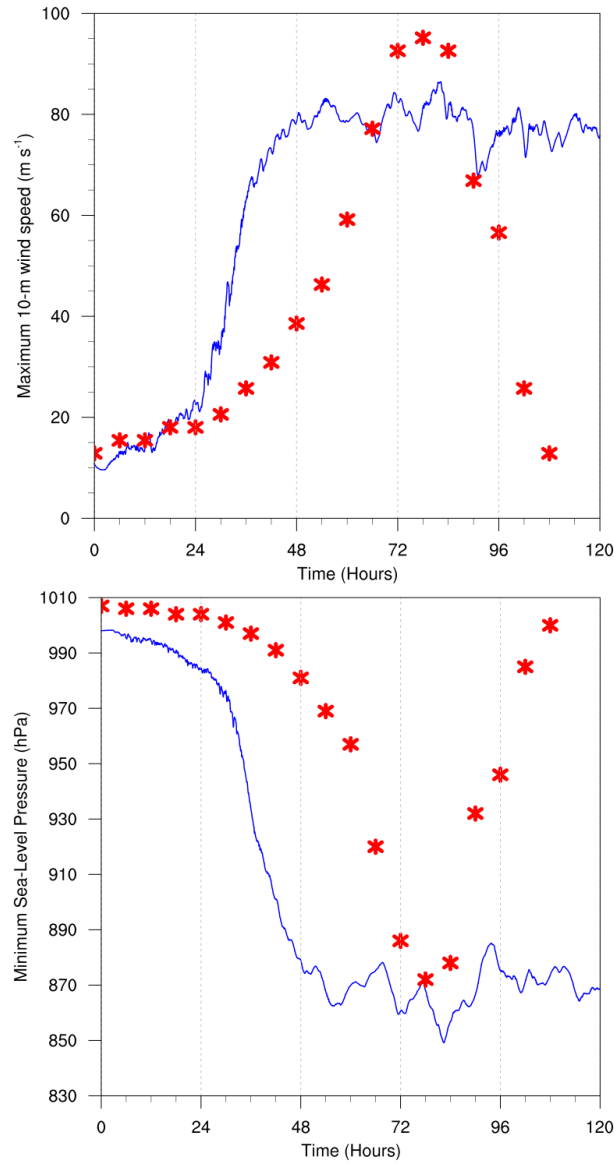


FIG. 1. The maximum 10-m wind speed (top panel;  $\text{m s}^{-1}$ ) and minimum sea-level pressure (bottom panel; hPa) in the simulated storm (blue lines) and from Hurricane Patricia's best track (red stars).

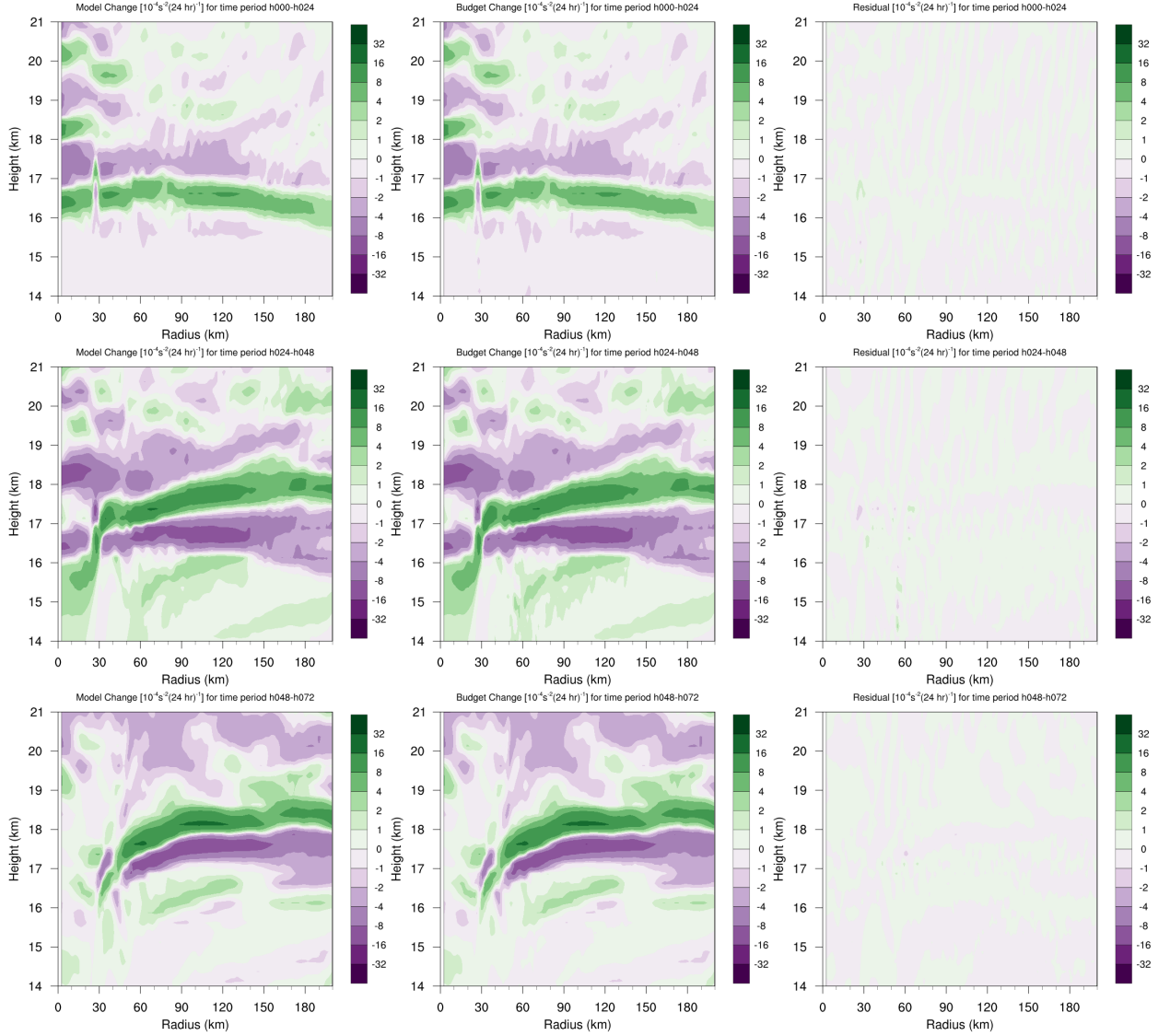


FIG. 2. Left panels: Twenty-four-hour changes in squared Brunt-Väisälä frequency ( $N^2$ ;  $10^{-4} \text{ s}^{-2}$ ) over (a) 0-24 hours, (b) 24-48 hours, (c) 48-72 hours, (d) 72-96 hours. Middle Panels: The  $N^2$  change over the same time periods computed using Eq. 6. Right Panels: The budget residual over the same time periods, computed by subtracting the budget change (middle column) from the model change (left column).

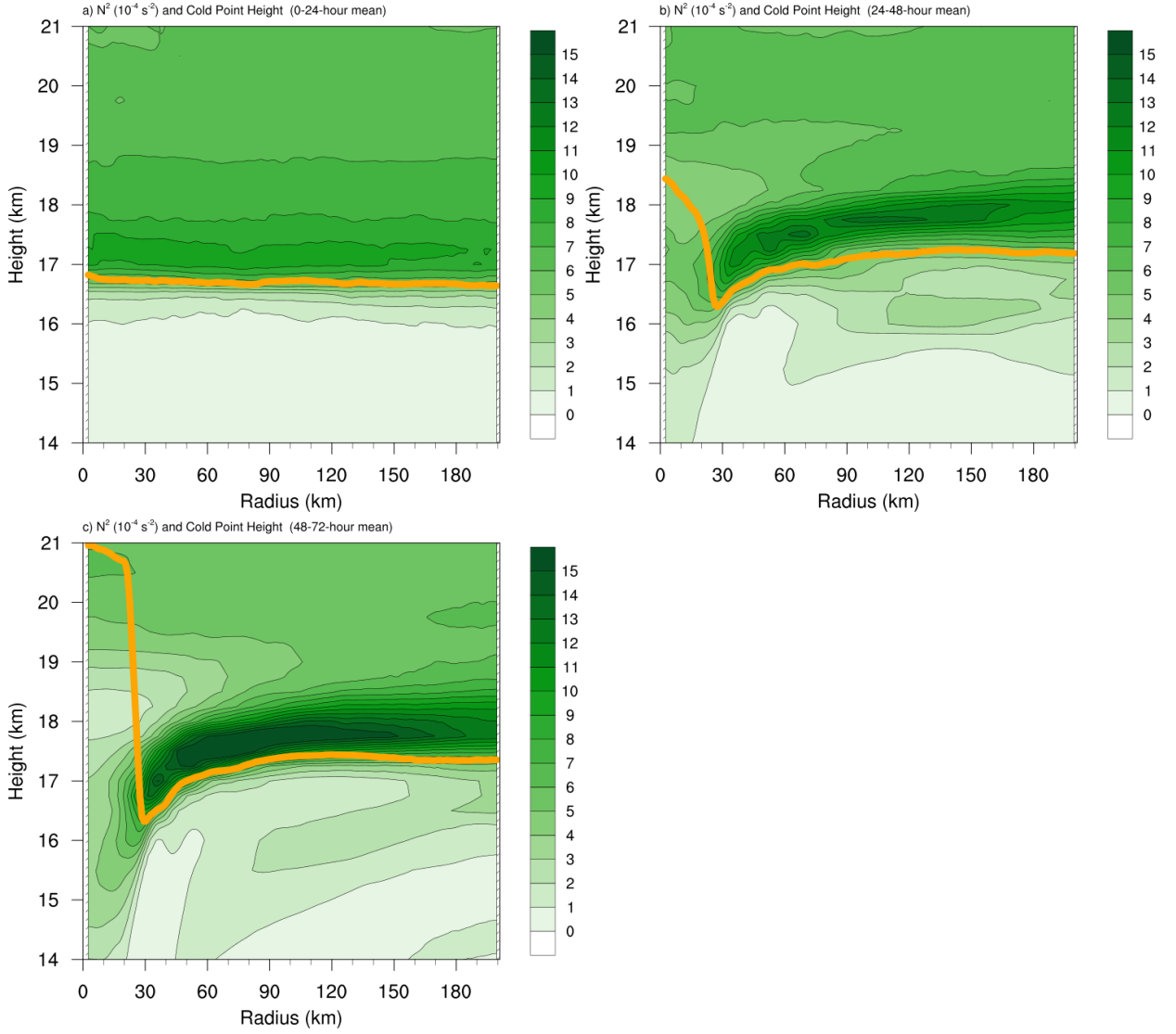
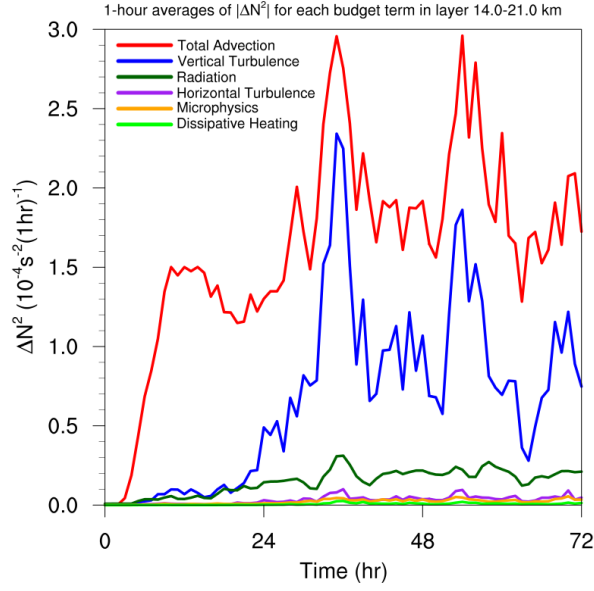


FIG. 3. Twenty-four-hour averages of squared Brunt-Väisälä frequency ( $10^{-4} \text{ s}^{-2}$ ) over the first four days of the simulation. Orange lines represent the cold-point tropopause determined by the mean temperature field over the same time periods.



291 FIG. 4. Time series of the contribution of each of the budget terms to the time tendency of the squared  
 292 Brunt-Väisälä frequency ( $N^2$ ;  $10^{-4} \text{ s}^{-2}$ ). For each budget term, the absolute value of the  $N^2$  tendency is averaged  
 293 temporally over 1-hour periods (using output every minute), and spatially in a region extending from 0 to 200  
 294 km radius and 14 to 21 km altitude.

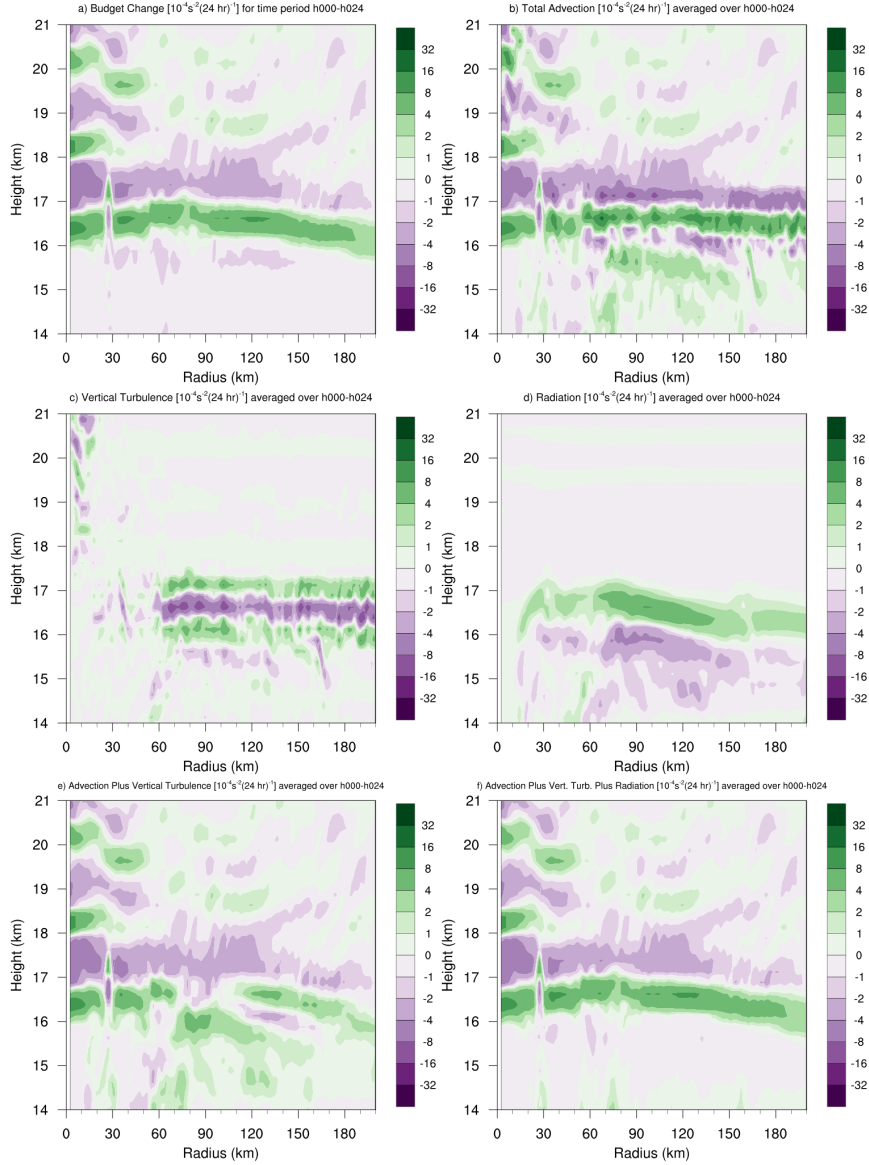


FIG. 5. (a) Total change in  $N^2$  over the 0-24-hour period ( $10^{-4} \text{ s}^{-2} (24 \text{ hr})^{-1}$ ) and the contributions to that change from (b) the sum of horizontal and vertical advection, (c) vertical turbulence, (d) longwave and shortwave radiation, (e) the sum of horizontal advection, vertical advection, and vertical turbulence, and (f) the sum of horizontal advection, vertical advection, vertical turbulence, and longwave and shortwave radiation.

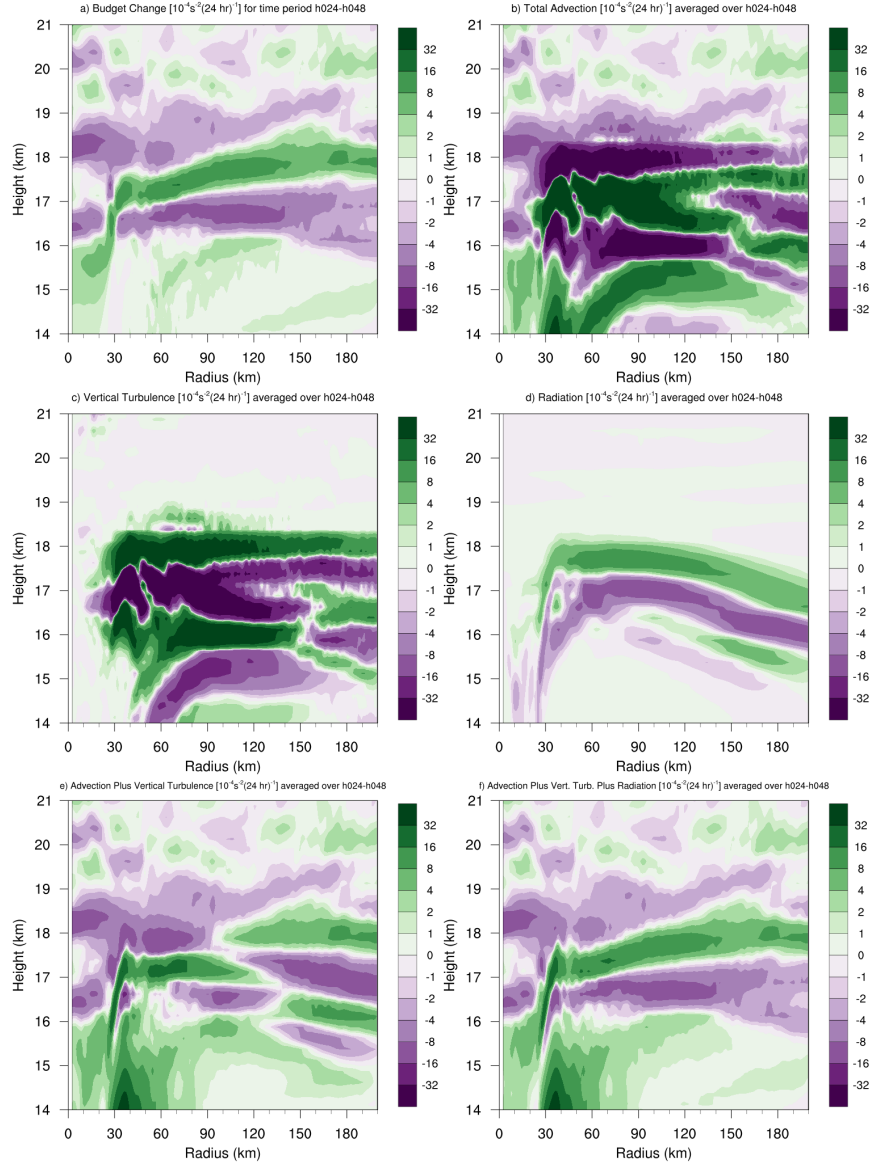


FIG. 6. As in Fig. 5, but for the 24-48-hour period.

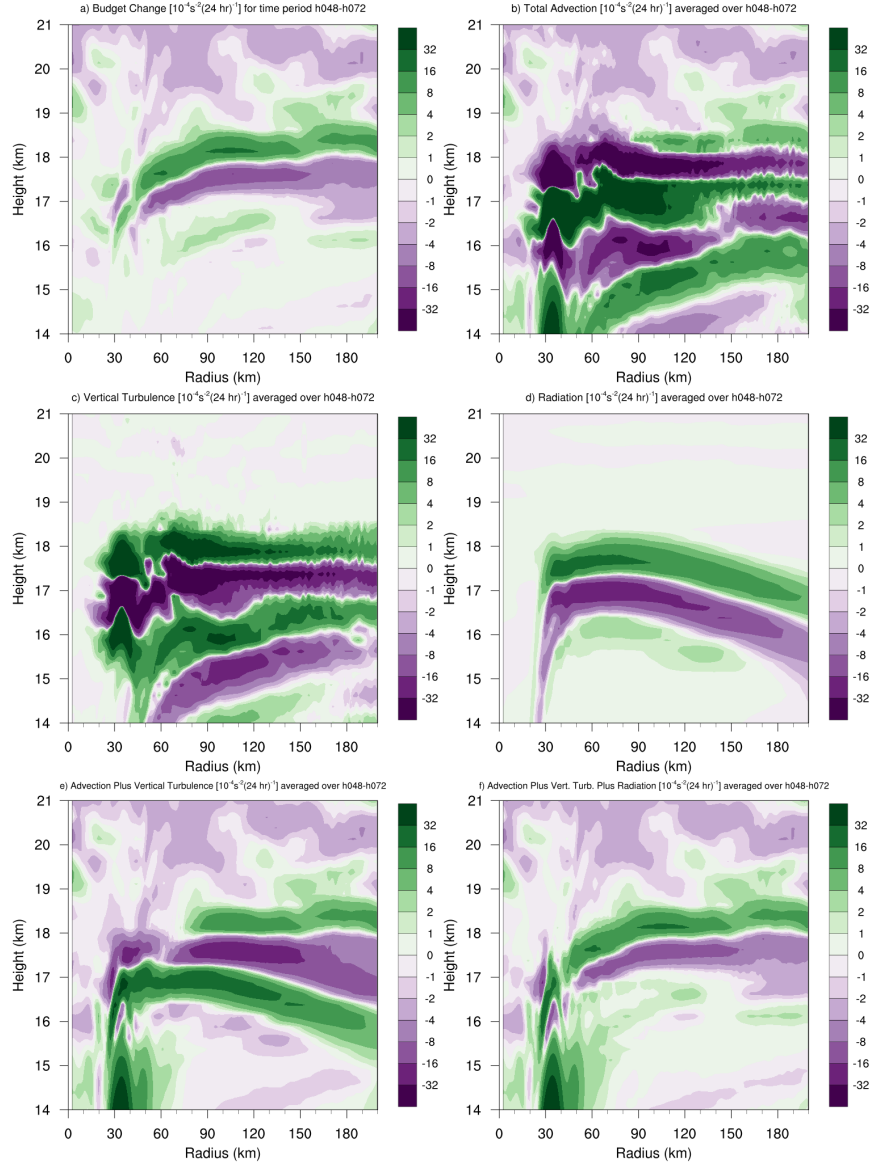


FIG. 7. As in Fig. 5, but for the 48-72-hour period.

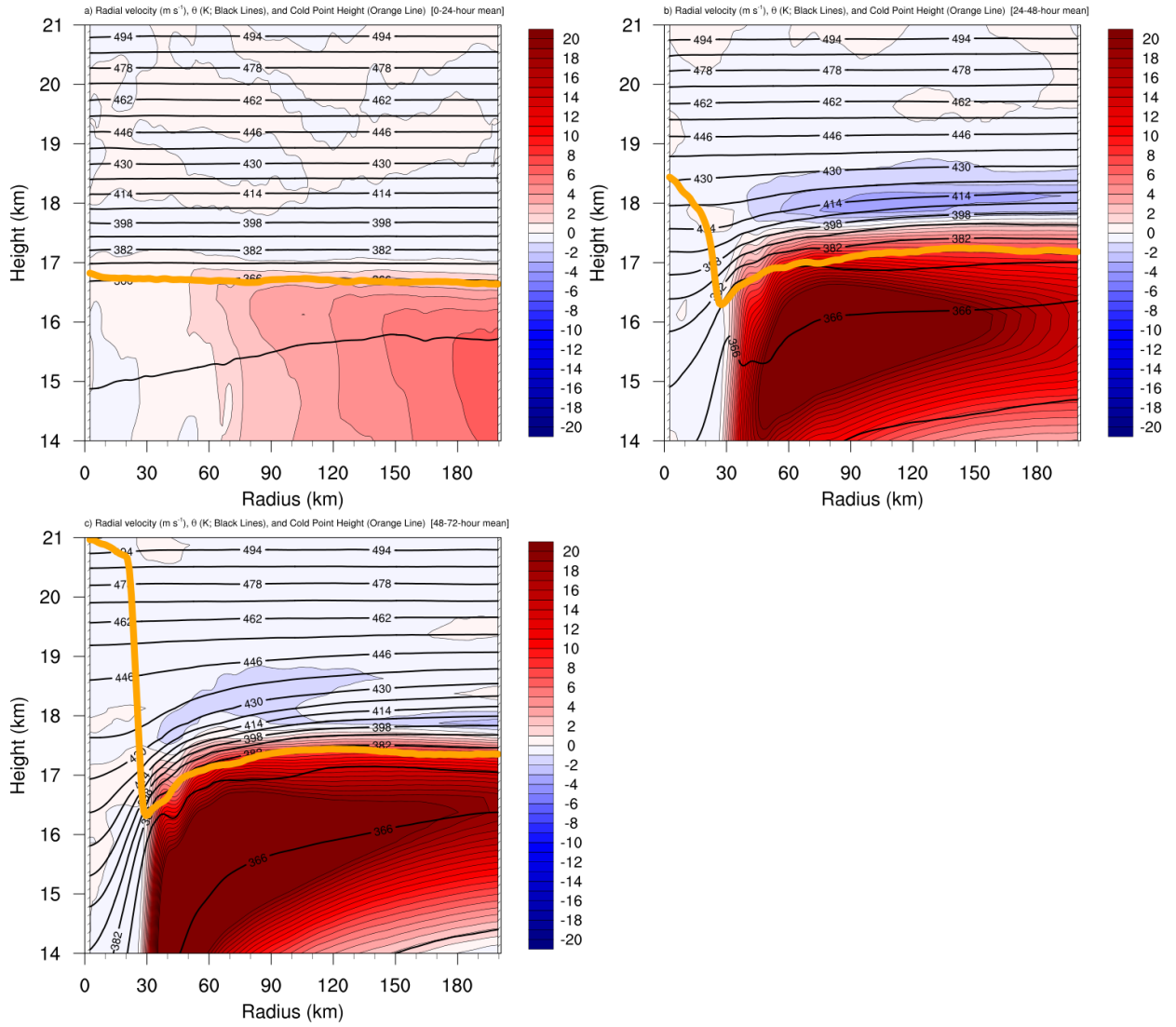


FIG. 8. Radial velocity ( $\text{m s}^{-1}$ ; filled contours), potential temperature (K; thick black contours), and cold point tropopause height (orange lines) averaged over (a) 0-24 hours, (b) 24-48 hours, and (c) 48-72 hours.



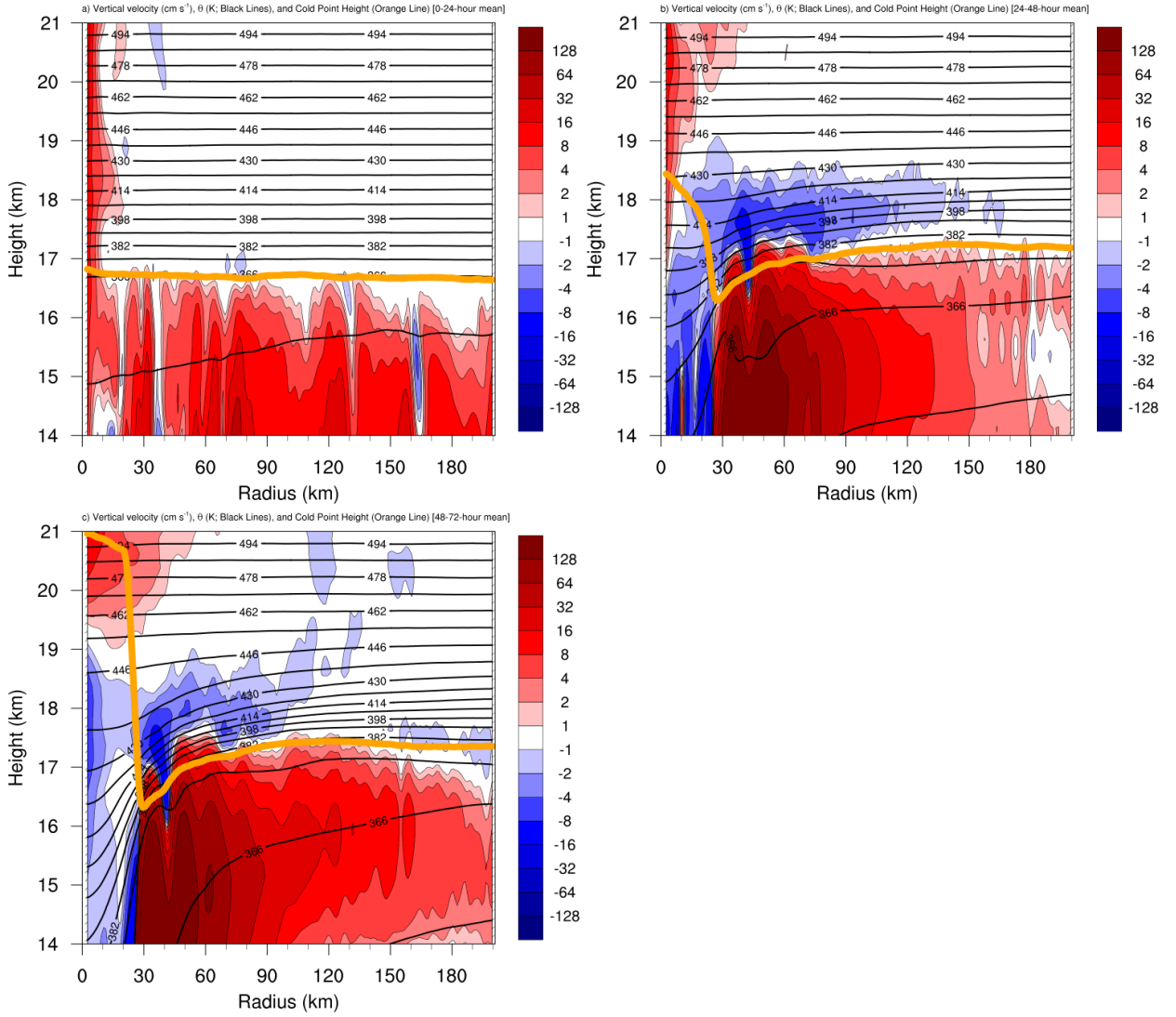


FIG. 9. Vertical velocity ( $\text{cm s}^{-1}$ ; filled contours), potential temperature (K; thick black contours), and cold point tropopause height (orange lines) averaged over (a) 0-24 hours, (b) 24-48 hours, and (c) 48-72 hours.

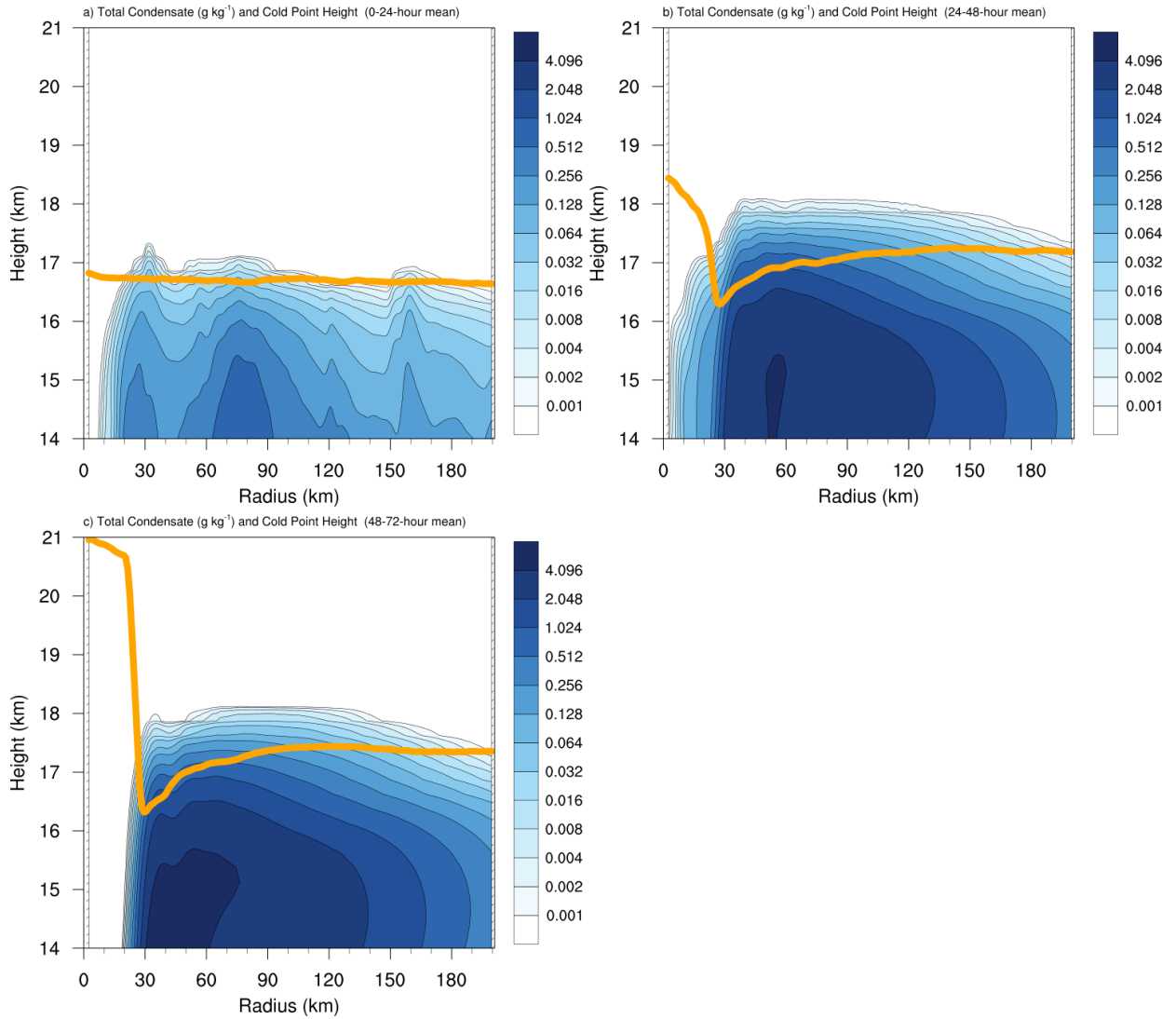


FIG. 10. Total condensate mixing ratio ( $\text{g kg}^{-1}$ ) and cold point tropopause height (orange lines) averaged over

(a) 0-24 hours, (b) 24-48 hours, and (c) 48-72 hours.

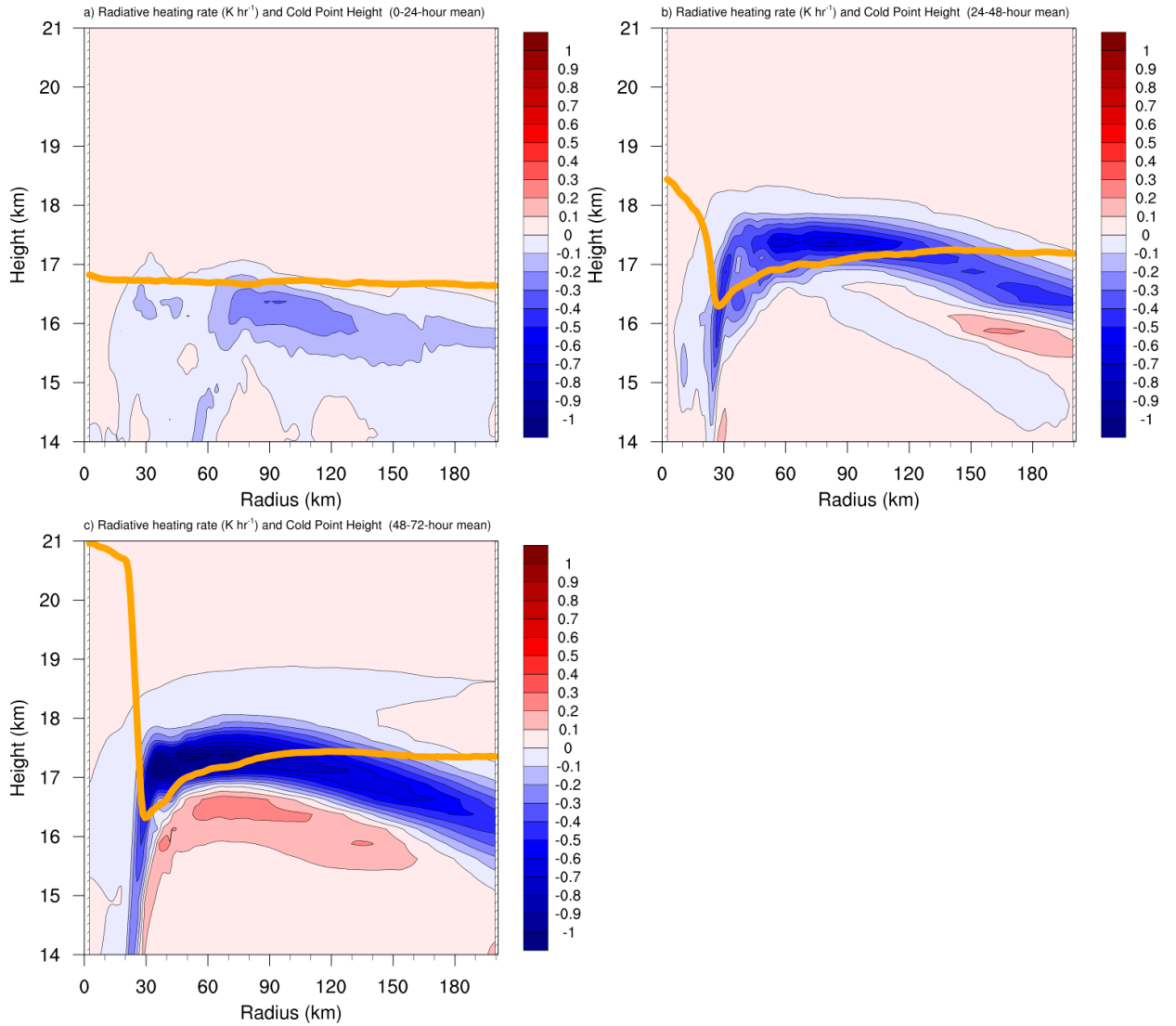


FIG. 11. Radiative heating rate ( $\text{K hr}^{-1}$ ) and cold point tropopause height (orange lines) averaged over (a) 0-24  
 hours, (b) 24-48 hours, and (c) 48-72 hours.

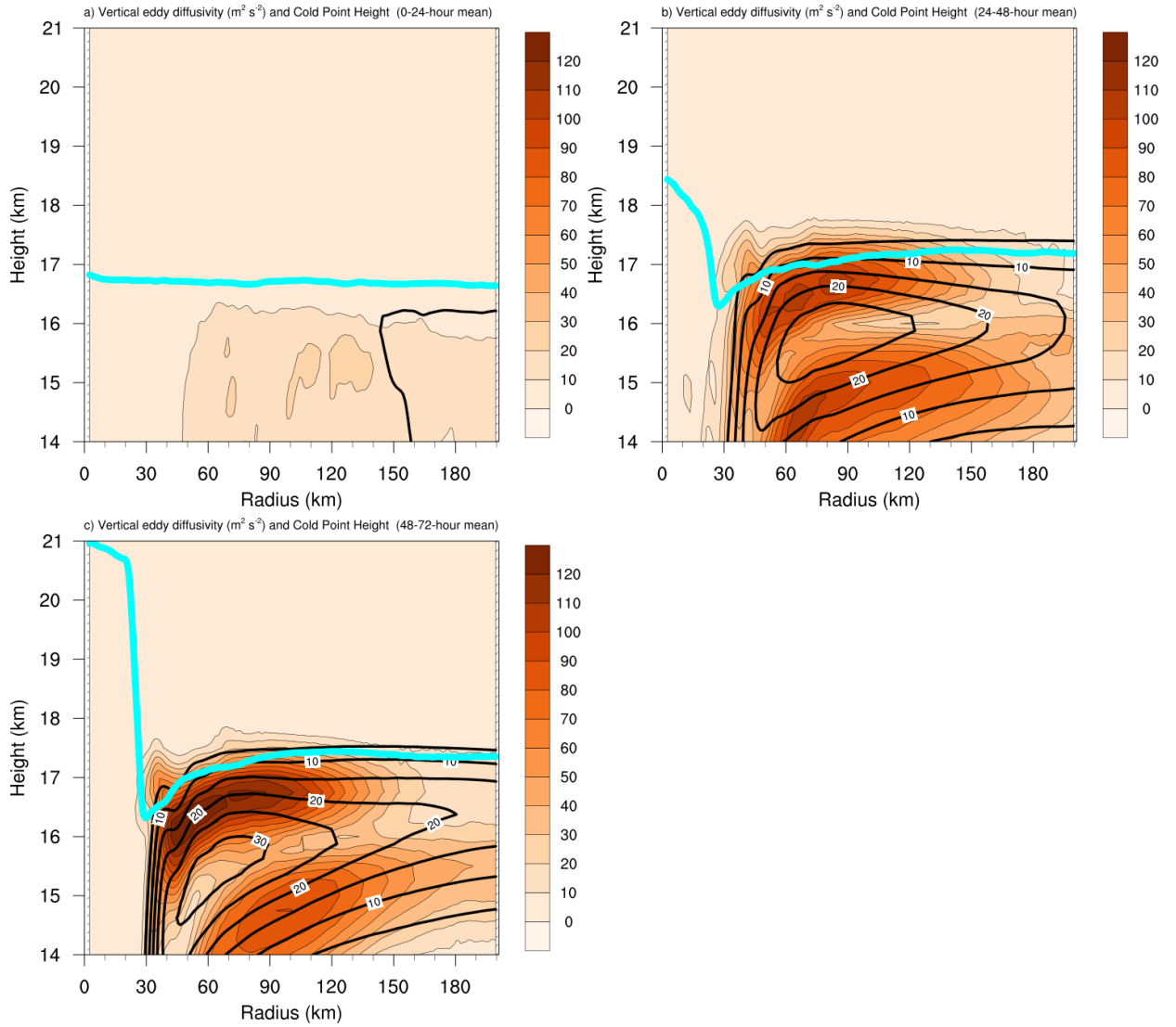


FIG. 12. Vertical eddy diffusivity ( $\text{m}^2 \text{s}^{-2}$ ; filled contours), cold point tropopause height (cyan lines), and radial velocity ( $\text{m s}^{-1}$ ; thick black lines) averaged over (a) 0-24 hours, (b) 24-48 hours, and (c) 48-72 hours.